Iranian Journal of Materials Forming 10 (2) (2023) 22-34

Online ISSN: 2383-0042

Iranian Journal of Materials Forming

Journal Homepage: http://ijmf.shirazu.ac.ir

Research Article

Effect of Severe Surface Plastic Deformation on Tribological Properties of CoCrWNi Super Alloys

R. Nemati[1], R. Taghiabadi[1*], M. Saghafi Yazdi[1] and S. Amini[2]

[1] Department of Metallurgy and Materials Science, Imam Khomeini International University, Qazvin, Iran
[2] Faculty of Mechanical Engineering, Department of Mechanical Engineering, Manufacturing and Production, University of Kashan, Iran

ARTICLE INFO

Article history:

Received 23 April 2023
Reviewed 29 May 2023
Revised 12 June 2023
Accepted 4 July 2023

Keywords:

L605
Friction hardening
Hardness
Sliding wear
Tribology

Please cite this article as:

R. Nemati, R. Taghiabadi, M. Saghafi Yazdi, S. Amini, Effect of severe surface plastic deformation on tribological properties of CoCrWNi super alloys, *Iranian Journal of Materials Forming*, 10(2) (2023) 22-34.

ABSTRACT

The effect of severe surface plastic deformation on the microstructure and tribological properties of CoCrWNi super alloy L605 was investigated. The surface of the annealed alloy was frictionally processed by a tungsten carbide tool with a tip radius of 5 mm under different sliding speeds of 500, 800, 1100, 1400, 1700, and 2000 mm/min for 2, 5, 10, 20, and 30 passes. Based on the results, applying friction hardening (FH) promoted the formation of the ε-HCP (martensite) phase in the surface structure of the γ-FCC alloy up to a depth of about 500 μm. The maximum surface hardness was observed at the sliding speed of 1700 mm/min and 30 passes, where the surface hardness increased by almost 100% (from about 320 HV to more than 635 HV). Pin-on-disk wear tests were carried out at room temperature, under applied pressures of 0.25, 0.5, and 1 MPa, for a sliding distance of 1000 m. According to the results, under low applied pressures, i.e. 0.25 MPa, the maximum wear resistance was observed in the sample FH-processed for 30 passes at 1700 mm/min. However, due to the formation of lateral microcracks on the surface of samples processed by high number of FH passes, under the applied pressure of 1 MPa, the lowest wear was observed in the 5-pass processed sample (1700 mm/min). The wear rate and average friction coefficient (AFC) of this sample were about 45% and 30% lower than those of the base (annealed) sample, respectively.

1. Introduction

Cobalt-chromium-tungsten-nickel L605 super alloy belongs to the Co-based heat-resistant alloys group. Owing to their high strength at elevated temperatures and excellent oxidation resistance (up to about 1100°C), these alloys are considered potential materials for the fabrication of parts used in the hot zones of gas turbines and aerospace industries [1]. These alloys also have excellent corrosion resistance and good biocompatibility which make them a good option for producing implants such as expandable stent-balloon [2], surgical implants [3], surgical fixation wire [4], heart valves, and cerclage cables. The wear and corrosion of implants due to chemical reactions and/or mechanical interactions can affect living tissues, biological systems, and organs and cause inflammation and blood coagulation restenosis [5].

* Corresponding author
E-mail address: taghiabadi@ikiu.ac.ir (R. Taghiabadi)
https://doi.org/10.22099/IJMF.2023.47206.1256

Therefore, because of the importance and wide range of applications in the manufacturing of implants, many efforts have been made to modify the surface structure/mechanical properties of L605 alloy.

Due to its very high work hardening rate, modification processes based on cold working were extensively used to improve the mechanical properties of L605 alloy. For instance, Abbasi et al. reported that after 5 to 35% cold rolling, the yield and tensile strengths of L605 alloy increased from 432 and 946 MPa to 1134 and 1334 MPa, respectively [6]. In addition, Arab et al. increased the hardness of L605 alloy from 321 to 542 HV through 20% cold upsetting [7]. Mechanical surface treatment processes such as grind hardening [8], hammering, shot peening, warm peening, stress peening, laser peening [9], deep rolling, and various types of burnishing processes such as ball burnishing [10], low plasticity burnishing, cryogenic burnishing, diamond burnishing, and ultrasonic burnishing [11] have also been used to modify the surface structure of Co-based alloys. Another category of mechanical surface modification processes based on cold working is machine hammer peening processes which use guided tools. These processes can be categorized into the processes with discontinuous tool-work contact such as ultrasonic peening (UP) and the processes with continuous tool-work contact such as ultrasonic nanocrystalline surface modification (UNSM), ultrasonic cold forging technology (UCFT), and ultrasonic burnishing [12].

The above-mentioned surface processing techniques usually require special and expensive equipment and have limitations regarding the shape and dimensions of the sample. Therefore, a very limited report exists regarding their impact on the surface properties of L605 alloy. In a study, Yang et al. performed cryogenic burnishing with liquid nitrogen on Co-Cr-Mo alloy and reported a hardness increase of about 87% (from about 300 HV to more than about 550 HV) [13].

FH is a relatively low-cost surface hardening technique that is done using common machining equipment without significant shape/dimensional limitations. In this method, the alloy surface is subjected to the loaded-sliding of a hard pin and experienced severe surface plastic strains to a depth of several hundred micrometers. The applied strains promote the formation of ultrafine grains and improve the surface mechanical and tribological properties [14]. Makaro et al. increased the temper resistance of quenched carbon steels containing 0.38, 0.51, 0.83, and 1.35 wt.% C by sliding a spherical-head pin (5 mm in diameter) under a normal load of 980 N [15]. In another research, Makaro et al. increased the microhardness of CK20 steel from 1.68 to 4.24 GPa at a depth of about 5 μm by sliding the side surface of a cylindrical tool (10 mm in diameter) under an applied load of 690 N [16]. In another work [17], a significant increase in the surface hardness of AISI 321 stainless steel was obtained through sliding a spherical diamond pin with a diameter of 3 mm, at a sliding speed of 50 mm/s, and applying a load of 392 N. According to the obtained results, when the number of passes changed from one to 11 passes, the alloy hardness increased from 560 to 710 HV (the initial hardness was 220 HV) and the volume percent of the martensite phase increased from 55 to 70%. Khaksaran et al. reported that FH led to martensitic phase transformation, a 180% increase in the hardness, and a 62% improvement in the wear resistance of 316L stainless steel [18]. Additionally, Shahriari et al. performed FH on Ti-6Al-4V alloy with different passes and sliding speeds. In their experiments, the hardness increased to a depth of more than 300 μm from 360 to 550 HV, and the wear resistance enhanced by more than 50% [14].

Considering the capabilities of the FH process in the improvement of surface mechanical properties of alloys and also the strain induced martensite transformation (SIMT) characteristics of L605 alloy, the present work aims to investigate the effects of FH on the microstructure, phase transformation, hardness, and tribological properties of L605 alloy.

2. Experimental Procedure

A sheet of the L605 alloy with a thickness of 6 mm was used in this research. The sheet was prepared by vacuum induction melting, electroslag refining, and finally hot rolling. The chemical composition of the sheet determined by atomic mass spectroscopy is presented in Table 1.

Table 1. Chemical composition of L605 alloy (wt.%)

Co	Cr	W	Ni	Fe	Mn	Si	C	P	S
Base	19.46	14.1	10.14	3.67	1.07	0.18	0.06	0.008	0.001

Samples with dimensions of 60×15×6 mm were prepared from the main sheet using a wire cut machine. The samples were solution annealed for 70 min in an AZAR-F11L-1250 electric furnace at 1200°C in the air atmosphere and then immediately quenched in water. Sliding FH was applied on the lateral surface of the samples with the dimensions of 6×45 mm using a cylindrical-head tungsten carbide pin with a 5 mm radius and 10 mm length (Fig. 1(a)). The process was carried out on a XIOS-ZAYER CNC milling machine. The sliding process was conducted at different speeds of 500, 800, 1100, 1400, 1700, and 2000 mm/min for 2, 5, 10, 20, and 30 passes. The setup and pictorial view of the process are shown in Fig. 1(b). At the start of the process, the tool was slid on the surface in the desired direction/speed. After traveling the predetermined distance, the sliding process was repeated in the reverse direction and continued until reaching the desired number of passes. It is worth noting that before applying each sliding pass, the tool was fed downward along the z-axis by 0.02 mm.

In order to approximate the applied load, the Abaqus stress analysis was performed. In this analysis. the boundary condition was applied at the bottom of the sheet. The tungsten carbide pin tool was considered as a rigid body and its interaction with the sheet surface was supposed to be a simple standard contact. Step analysis was used as a dynamic implicit. The results were extracted based on a linear element with quadratic shape and the mesh size was reduced up to 0.08 mm in order to improve the precision of the data in the contact point. The vertical displacement distribution map in Fig. 2(a) depicts the situation in which the pin tool has indented into the surface by about 0.02 mm. The top surface of the pin was coupled to its center and the displacement of 0.02 mm was applied to this point in vertical direction. In this condition, the reaction force for the coupled node was determined to be about 2800 N. Moreover, depending on the number of FH passes, the material is likely to be accumulated in front of the pin and removed from the surface in the form of small chips (Fig. 2(b)).

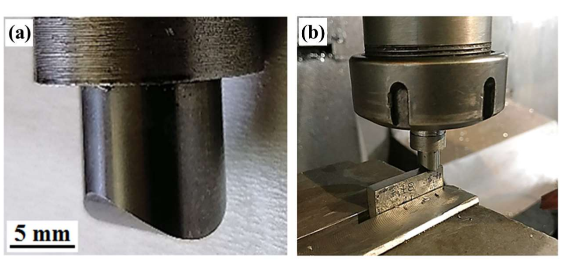

Fig. 1. (a) Cylindrical-head WC pin tool, and (b) setup of the FH process.

The FHed samples are indicated by a two-part number system as XXXX-XX. The first part refers to the sliding speed (mm/min) and the second part (after dash) denotes the number of passes.

The surface preparation was performed according to the standard metallographic procedures. The surfaces were chemically etched by a 20 ml HCL- 1 ml H_2O_2 solution for 40 s to reveal the microstructure in a direction parallel to the sliding direction. The structure

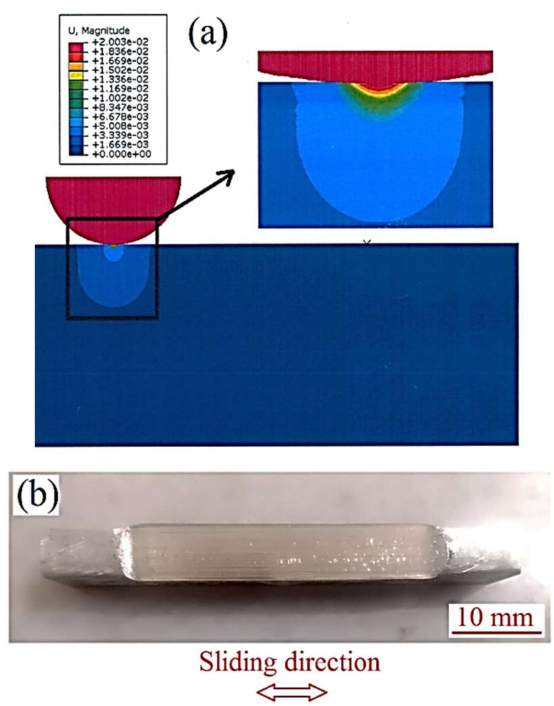

Fig. 2. (a) Vertical displacement distribution map, and (b) a typical FHed surface.

of the samples was examined by an Examet Union 81892, OSK optical microscope (OM). A MIRA3 TESCAN scanning electron microscope (SEM) equipped with an EDS detector was also used for the elemental analysis of the worn surfaces and debris. The image analysis of the microstructure and wear debris was performed using the Digimizer 5.3.5 software.

The hardness of the samples was determined according to the ASTM E84 standard using a micro hardness tester (SHAAB, Model MS) under the applied load of 100 g and a dwelling time of 10 s. The X-ray diffraction test was performed with a copper cathode lamp with $K_{\alpha 1}$ rays at a wavelength of 1.54060 Å, with a scanning angle step of 2θ = 0.02° and a scanning time of 0.8 s. The pin-on-disk room temperature sliding wear tests were performed according to ASTM G99 using a TR-20 DUCOM tribometer at a sliding speed of 0.2 m/s, applied pressures of 0.25, 0.5, and 1 MPa, at a distance of 1000 m. The flat-end cubic pins with dimensions of 6×6×15 mm were used against an alumina disk. Before each test, the samples were ultrasonically cleaned in acetone.

3. Results and Discussion

3.1. Hardness testing results

The effect of the sliding speed and the number of passes on the Vickers hardness of FHed samples at a depth of about 50 μm below the processed surface is shown in Fig. 3. As seen, irrespective of the process parameters, FH substantially increased the surface hardness of the L605 alloy. Moreover, at a given sliding speed, increasing the number of FH passes led to a continuous increase in the alloy hardness. The hardness of the 1700-30 sample was 20% higher than that of the 1700-2 sample. This could be attributed to the accumulation of strain hardening at each pass.

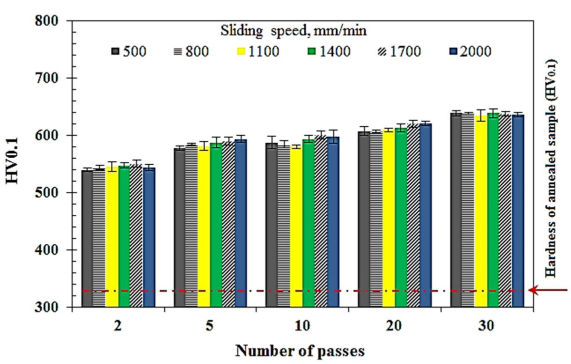

Fig. 3. The variation of the hardness of L605 alloy (at a depth of about 50 μm from the processed surface) against the number of FH passes for different sliding speeds.

Due to increasing the sliding-induced surface shear strains and accordingly the enhanced dislocation accumulation [19], augmenting the sliding speed due to increasing the local strain rate is expected to increase the flow stress/hardness, substantially [20]. It is worth noting that during the sliding friction, the outermost layers of sliding surfaces experience high strain rates in the range of about 10^3/s (and a little more) [21] which can result in the hardness growth. However, as shown in Fig. 3, at a given number of FH passes, the sliding speed had a marginal effect on the hardness of L605 alloy. According to Fig. 4(a) which shows the hardness profiles of 500-30 and 1700-30 samples, for an increase of about

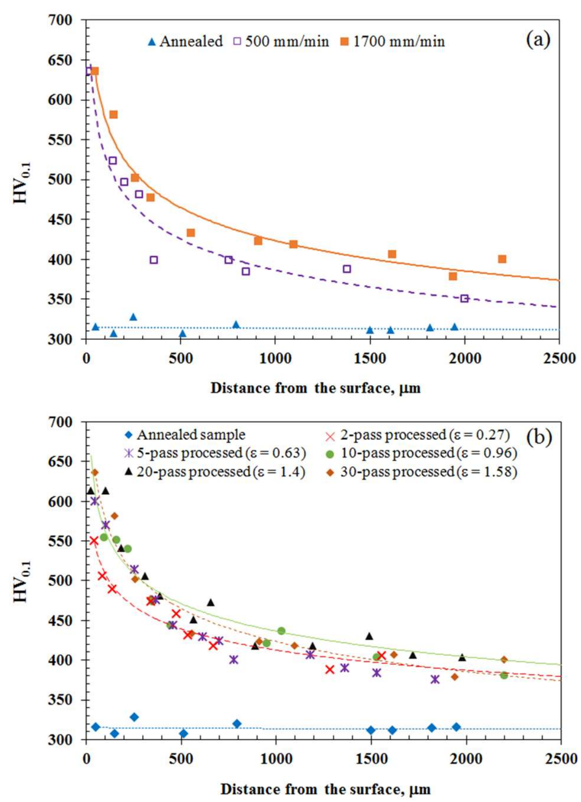

Fig. 4. Hardness profiles showing (a) effect of FH sliding speed at 30 passes, and (b) effect of the number of FH passes at the sliding speed of 1700 mm/min. The equivalent shear strain values at a depth of about 50 μm below the processed surfaces are shown on Fig. 4(b).

240% in the sliding speed, the hardness only improved by about 10%. Nevertheless, several previous studies reported the positive effect of the FH tool sliding speed on the hardness improvement of alloys. According to Shahriari et al. [14], an increase in the FH sliding speed from 45 to 720 mm/min, increased the surface hardness of a 30-pass processed Ti-6Al-4V alloy from 375 to about 500 HV. This improvement was attributed to increasing the fraction of the martensite phase in the surface areas. No improvement in the hardness was observed at higher sliding speeds. In another study on the effect of FH on the hardness and tribological properties of 316L steel, Khaksaran et al. [18] reported an increase in the hardness with the tool sliding speed. This contradiction in the results may be explained by the hardness saturation phenomenon whose occurrence during severe plastic deformation of the alloys was attributed to the saturation of dislocations in the grains [22], the saturation of martensite [23], and the balance between the accumulation and recovery of dislocations [24].

Considering the above discussion, the sliding speed of 1700 mm/min was chosen as the optimum processing speed for further investigations. The hardness profile of the 1700-XX samples is presented in Fig. 4(b). As seen, the surface hardness of FHed L605 alloy increased up to a distance of 500 μm from the surface. It can also be seen that due to the shear strains applied and the alloy work hardening the surface hardness of 1700-2, 1700-5, 1700-10, 1700-20, and 1700-30 samples is about 70, 85, 88, 94, and 100% higher than that of the annealed sample. The equivalent value of subsurface strain (ε) can be calculated by the following equation:

$$\varepsilon = \frac{\sqrt{3}}{3}\tan\theta \quad (1)$$

where θ (in radians) is the shear angle between grain boundaries and the normal to the surface [25].

3.2. Microstructural examination

The annealed microstructure of L605 alloy and subsurface microstructure of 1700-2 and 1700-5 samples are shown in Figs. 5(a) and 5(b), respectively. The base microstructure consisted of large polygonal grains and a large number of annealing twins, typical of low stacking-fault energy materials [26] (Fig. 5(d)), whilst the subsurface microstructure of FHed samples consisted of a severely deformed fine-grained microstructure in which the original annealing twins were severely distorted (Figs. 5(b)). Annealing twins are usually formed in recrystallized microstructure through grain growth or grain boundary dissociation processes [26]. It is also evident from these figures that increasing the number of FH passes increased the depth and intensity of plastically deformed layers beneath the surface.

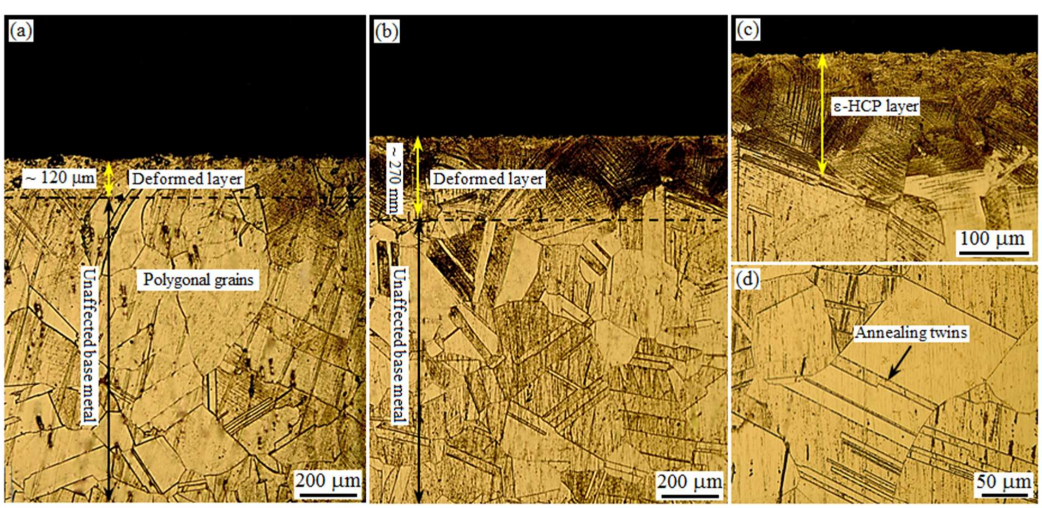

Fig. 5. Subsurface microstructure of (a) 1700-2, and (b) 1700-5 FHed samples. (c) and (d) are enlarged views of the FHed zone and unaffected base metal of 1700-5 sample, respectively.

To better examine the effect of FH on the microstructure, X-ray diffraction was performed on the annealed and 5-pass hardened alloys. The results are presented in Fig. 6. As seen, the annealed sample displayed diffraction peaks corresponding to the γ-FCC structure at 2θ angles of 43°, 50°, and 75°. In the FHed samples, new peaks corresponding to ε-HCP martensite phase appeared at two angles of 47° and 62°, while the intensity of the γ-FCC peak (at the angle of 50°) decreased. These findings are in accordance with the observations of Wang et al. on Cr-Cr-W-Ni alloys who demonstrated the existence of x-ray diffraction peaks representing a composite microstructure composed of γ-FCC and ε-HCP phases at the same angles [27]. Therefore, the annealed sample has an FCC structure, and the hardened samples have a mixed microstructure comprising of both FCC and HCP phases. The FCC to HCP transformation occurred on the deformed layer up to a depth of about 500 µm from the processed surface. According to [28, 29], the annealing twins, and to a much lesser extent, the grain boundaries are suitable sites for the nucleation of ε-HCP martensite.

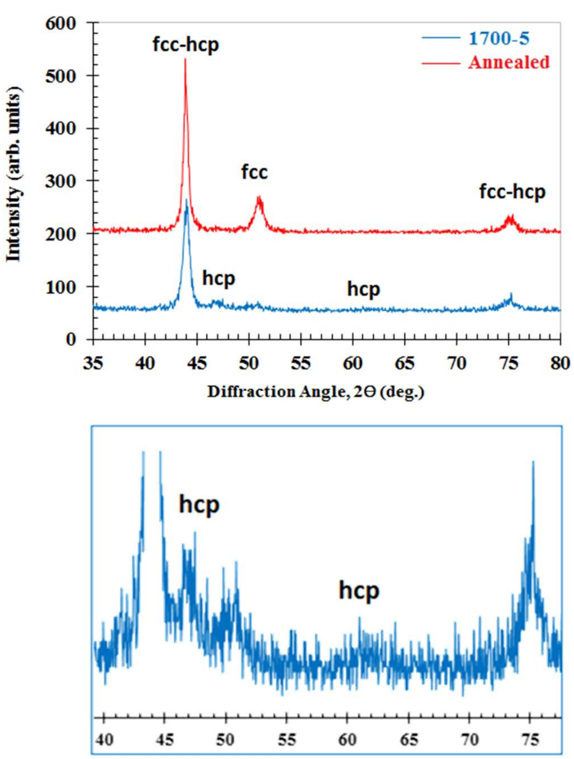

Fig. 6. XRD patterns of the annealed and 1700-5 FHed sample.

Therefore, besides the dislocation strengthening caused by cold work storage of dislocations [30], SIMT can be regarded as another important hardening mechanism in FH-processed alloys (Figs. 5(b) and 6). The formation of ε-HCP martensite plates caused by overlapping/coalescence of stacking faults [31, 32] can enhance the alloy hardness (Fig. 3) and their positive impact on the wear resistance of CoCrMo alloys was demonstrated previously [33]. However, several authors showed that the nucleation and propagation of microcracks at the semi-coherent interface of the ε-HCP/γ-FCC could greatly impair the tensile properties of Co-based superalloys [6, 29, 33]. Evidence of this phenomenon has also been found in the current research, which will be further discussed. Indeed, due to the low stacking fault energy, L605 alloy exhibits wider stacking faults which makes it difficult for the dislocations to cross slip and climb; i.e. lowering the dislocation mobility [34].

The grain boundary strengthening, and the grains subdivision associated with a high density of SFs [32] were also proposed as other mechanisms responsible for the hardening of the FHed samples. However, based on the calculations made by Williamson-Hall method, probably due to the continuous removal of the deformed layer in the form of debris, the size of the grains in the annealed and FH processed samples were similar.

3.3. Tribological properties

The variation of the wear rate of the base (annealed) and FHed samples (1700-XX samples) with the number of FH passes at different applied pressures is shown in Fig. 7. In order to investigate the samples' wear in conjunction with their hardness, the Vickers hardness of the samples was also included on the diagram. According to the results, under the applied pressure of 0.25 MPa, the wear rate of FHed samples decreased by increasing the number of the processing passes. The wear rate of 1700-2, 1700-5, 1700-10, 1700-20, and 1700-30 samples were lower than that of the base sample by about 16, 36, 50, 64, and 66%, respectively. Similarly, under the applied pressure of 0.5 MPa, as the

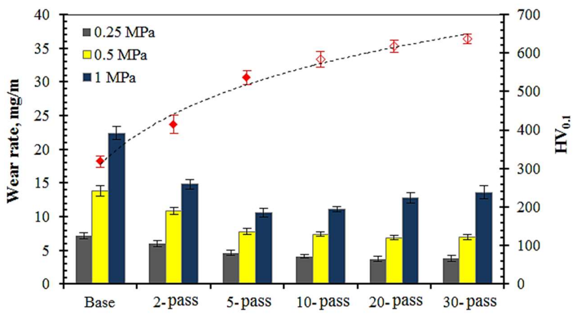

Fig. 7. Variation of wear rate and surface hardness of L605 alloy against FH passes.

number of FH passes increased to 5, the wear rate decreased by about 44%. When the number of passes exceeded 5, the wear rate remained almost constant. Under an applied pressure of 1 MPa, the wear rate of the alloy decreased (by about 52%) with FH passes (up to 5 passes). Thereafter, it slightly increased with further increasing the number of passes.

In order to investigate the FH effect on the wear behavior of L605 super alloy and to explain the related wear mechanisms, the worn surfaces and wear debris were examined/analyzed by SEM. Fig. 8 shows the worn surface morphology of the base alloy after 1000 m wearing under the applied pressure of 0.5 MPa. The EDS analysis of the worn surface is also presented in Fig. 9.

According to Fig. 8 and the EDS analyses presented in Fig. 9, the worn surface of the base sample was covered by an oxide-rich tribolayer which experienced considerable delamination as the dominant wear mechanism. Tribological layer is a layer that is formed due to the chemical/mechanical mixing and compression of solid particles generated during the wear of both surfaces [35, 36]. Considering its composition (high oxide content) and porous nature, it is expected that its formation significantly reduces the friction and adhesion between the contacting surfaces [37]. This is due to the fact that the tribolayer reduces the possibility of direct contact and the occurrence of cold welding between the surface asperities. However, considering the similarity of the chemical composition of point A (inside the delaminated crater) and point B (outside the delaminated zone) (Fig. 9), it seems that the delamination-related microcracks propagate through the tribolayer. Therefore, the material removal is limited to the tribological layer.

Examining the average size (74.2±36.4 µm) and morphology of the wear debris produced during wear of the base sample (Fig. 10(a)) also indicates the delamination and relatively severe wear of the tribolayer.

The morphology of the worn surfaces of 1700-5, 1700-10, and 1700-30 samples after sliding under the applied pressure of 0.5 MPa is shown in Figs. 11a-11c, respectively. As can be seen, compared to the base sample (Fig. 8), the worn surface of the 1700-5 sample

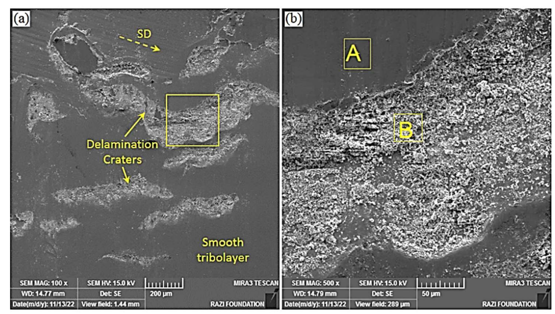

Fig. 8. (a) SEM images showing the worn surface of the annealed alloy after wearing under the applied pressure of 0.5 MPa, (b) Enlarged view of the boxed area in micrograph (a). Sliding direction is shown by an arrow.

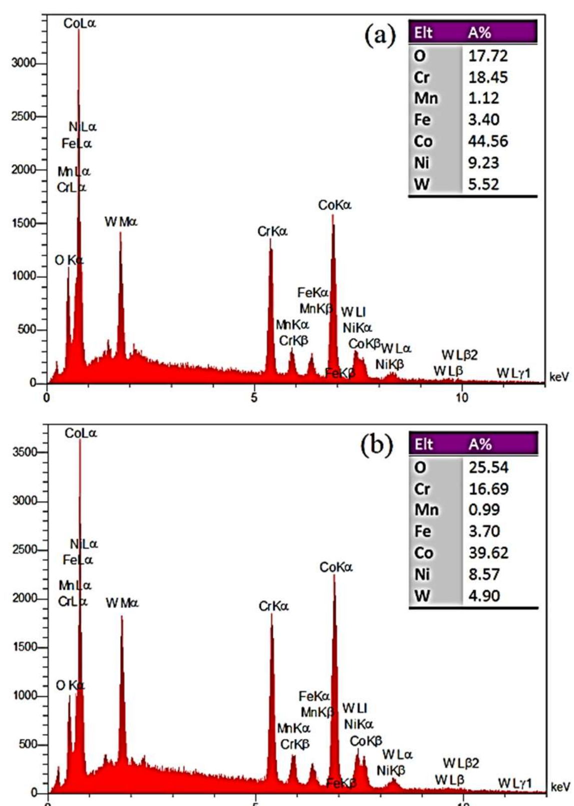

Fig. 9. EDS analysis of the marked areas in Fig. 8(b), (a) zone A, and (b) zone B.

was covered by a stable and compact tribolayer (with the chemical analysis presented in Fig. 12) with small pits/craters and shallow abrasion grooves in the sliding direction. The significant reduction in the size of the pits/craters on the worn surface and an increase in the wear resistance of 1700-5 sample (Fig. 7) can be attributed to the increased hardness of its substrate as compared to the base sample (approximately 70% higher). In confirmation of the previous studies [38, 39], increasing the substrate hardness lowers the amplitude/depth of the friction-induced surface plastic deformation and enhances its ability to support the tribolayer. The parallel grooves formed on the worn surface of the 1700-5 sample also originated from the

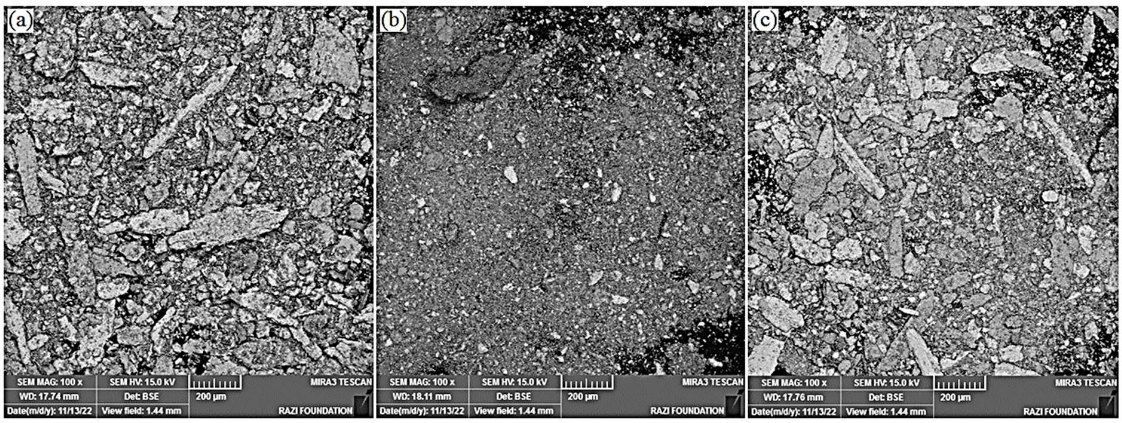

Fig. 10. SEM images showing the wear debris morphology of (a) base (annealed), (b) 1700-5, and (c) 1700-30 FHed samples. Applied pressure was 0.5 MPa.

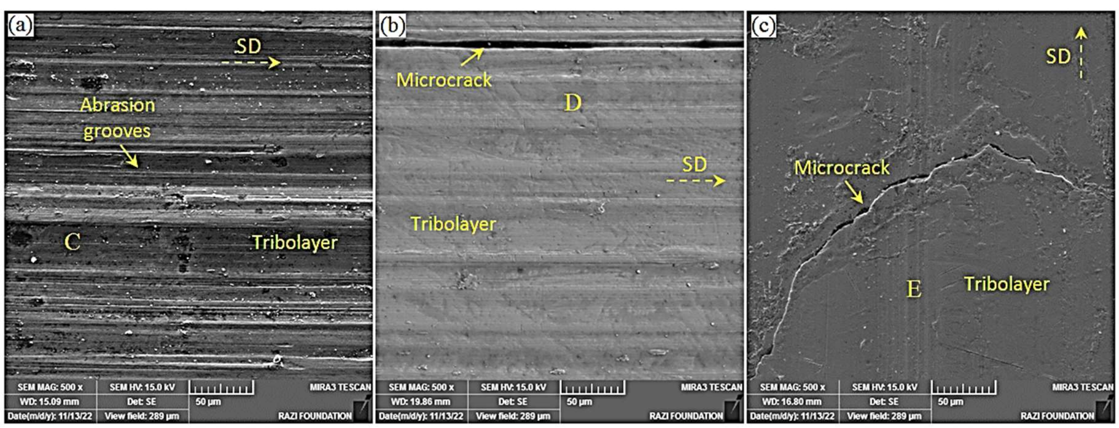

Fig. 11. SEM images showing the worn surfaces of (a) 1700-5, (b) 1700-10, and (c) 1700-30 FHed samples. The sliding direction is shown on the micrographs by the arrow.

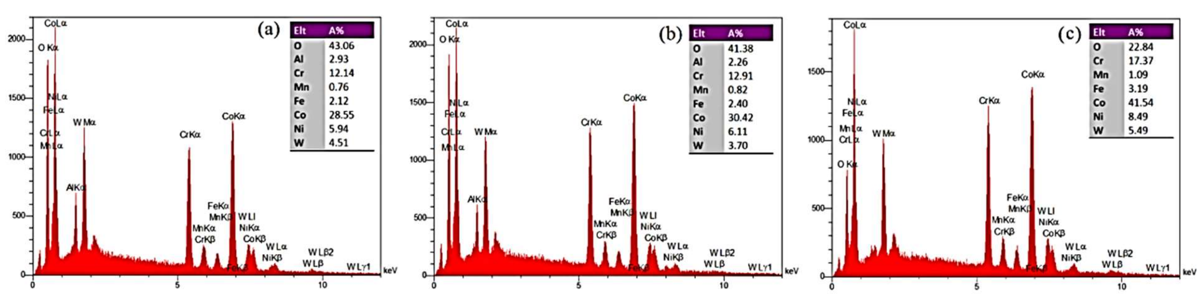

Fig. 12. EDS analysis of the marked areas on Fig. 11, (a) zone C, (b) zone D, and (c) zone E.

three-body abrasion by the hard debris involved between sliding surfaces. The size distribution (average size of 8.8±6.1 μm) and morphology of the wear debris of the 1700-5 sample, after sliding under the applied pressure of 0.5 MPa, is shown in Fig. 10(b). As can be seen, in agreement with the wear results (Fig. 7) and the morphology of the worn surface (Fig. 11(a)), the wear debris were composed of small-sized equiaxed particles. Therefore, mild tribolayer delamination/abrasion can be considered as the dominant wear mechanism in the 1700-5 sample.

According to the well-known Archard equation [40], the wear rate of an alloy is inversely proportional to its hardness. However, according to the obtained results, despite a 70% increase in the hardness of the 1700-5 sample compared to the base, its wear rate only increased by 36, 44, and 53% under three applied pressures of 0.25, 0.5, and 1 MPa, respectively. This deviation could be explained by the high work hardening rate of the experimental alloy and the probable increase in the alloy hardness during the sliding wear which could enhance its wear resistance. The measurements showed that after 1000 m of sliding under the applied pressure of 0.5 MPa, the bulk hardness of the annealed sample (317 $HV_{0.1}$) increased to 470, 350, and 280 $HV_{0.1}$ at the surface and the depths of 35 and 125 μm from the worn surface, respectively.

Increasing the number of FH passes to more than 5 increased the alloy hardness (Fig. 7). However, its effect on the wear resistance seems to depend on the applied pressure. Examining the worn surfaces of the 1700-10 and 1700-30 samples, after wearing at the applied pressure of 0.5 MPa (Figs. 11(b) and 11(c), respectively), depicts the formation of a dense and smooth tribolayer with the EDS analysis shown in Figs. 12(b) and 12(c), respectively. The formation of a protective tribolayer on the worn surface is most likely due to the high substrate resistance against the sliding-induced plastic flow which enhances its potential to support the tribolayer and gives it more time to become smoother and denser. However, based on the wear data (Fig. 7) under the applied pressures of 0.25 and 0.5 MPa, the wear rate of 1700-10 and 1700-30 samples was slightly lower than that of the 1700-5 sample, while at the applied pressure of 1 MPa, the wear resistance of the samples became slightly worse. This implies that something probably reduced the strength of the substrate.

To better investigate this issue, the surface morphology of the base and selected FHed samples were examined by a stereo OM (Fig. 13). As seen, increasing the number of FH passes over 5 led to the formation of lateral surface cracks and pits, the density/severity of which increased by increasing the number of FH passes. The formation of lateral cracks on the as-FHed surface of CK20 steel was demonstrated by Makaro et al. [16]. Regarding the industrial importance, much research was conducted to investigate the cold-work related microcracking in Co-based superalloys. It was found that microcracking generally occurred along the weak semi-coherent interface between the ε-HCP and γ-FCC phases [41]. According to [34], during the cold work deformation, the rupture is likely to initiate from {111} and {0001} planes of FCC and HCP phases, respectively.

The subsurface microstructure of the 1700-5 and 1700-30 samples after wearing at the applied pressure of 1 MPa is shown in Figs. 14(a) and 14(b), respectively. The formation of a subsurface microcrack is evident on the substrate of 1700-30 sample which can be correlated to the propagation of already nucleated microcracks at the ε-HCP/γ-FCC interface [41]. It seems that the gradual propagation of subsurface microcracks towards the wear surface destabilized the tribolayer and provoked more severe wear by intense tribolayer delamination which manifests itself as the formation of high fractions of large (average size of 63.1±31.5 μm) flaky wear particles (Fig. 10(c)).

The variation of the AFC with sliding distance of the base, the 1700-5 and 1700-30 samples (applied pressure of 0.5 MPa) is illustrated in Fig. 15. As can be seen, the friction coefficient of the base alloy had a significant fluctuation. In accordance with the wear result (Fig. 7) and wear surface morphology (Figs. 8 and 11), such fluctuation can be attributed to the instability (severe delamination/abrasion) of the tribolayer.

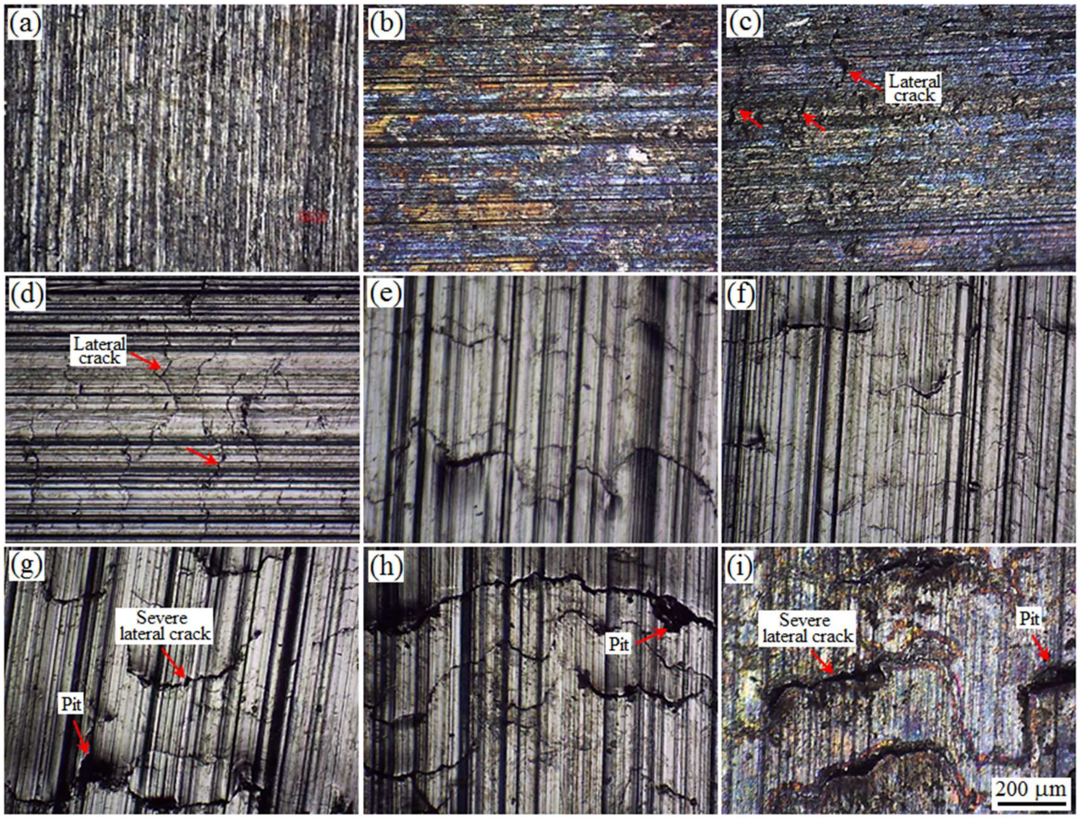

Fig. 13. Stereo OM images showing the surface morphology of (a) base (annealed), (b) 1700-5, (c) 1700-10, (d) 1700-20, (e) 1700-30, (f) 500-20, (g) 1100-20, (h) 2000-20, and (i) 800-30 FHed samples.

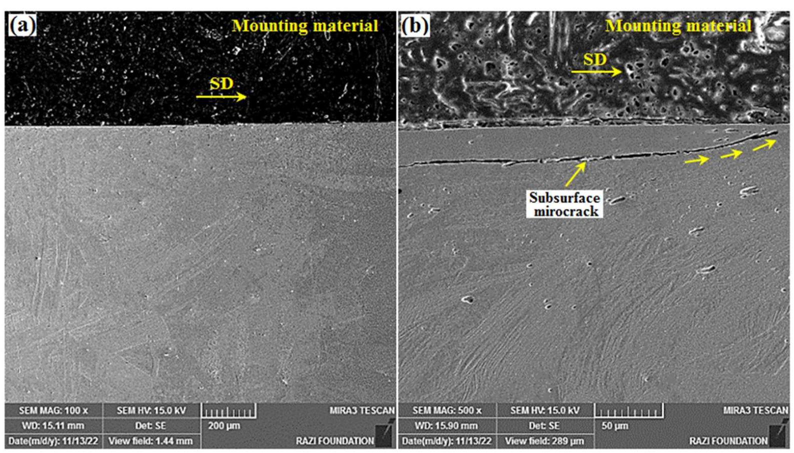

Fig. 14. SEM images showing the cross section of (a) 1700-5, and (b) 1700-30 FHed samples. The propagation of subsurface cracks towards the surface in the 1700-30 sample is quite evident. The sliding direction (SD) is indicated by arrows on the figures.

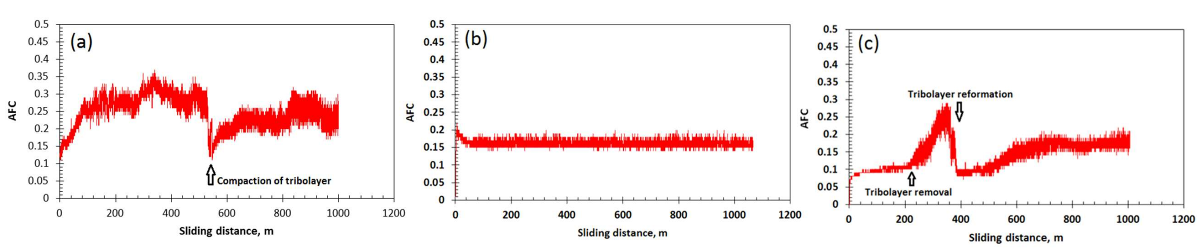

Fig. 15. Friction coefficient diagrams of (a) base (annealed), (b) 1700-5, and (c) 1700-30 samples.

The AFC diagram corresponding to the 5-pass FHed sample is shown in Fig. 15(b). As can be seen, due to the presence of a dense and compact tribolayer on its surface, the possibility of the adhesion between the sliding surfaces and, as a result, the abrasion component of the friction coefficient must be reduced. Therefore, the AFC of this sample was about 33% lower than that of the base sample. Besides, the frictional behavior of this sample was very stable, and the fluctuation range was about 78% lower than the fluctuation ranges observed in the friction coefficient of the base sample. By increasing the number of passes up to 30, the friction behavior of the sample changed drastically (Fig. 15(c)). As can be seen, the AFC of this sample was about 10% less than the 5-pass sample, but its friction coefficient fluctuation range was about 3 times that of the 5-pass sample. According to Fig. 11(a), the reduction of the friction coefficient of this sample compared to sample 1700-5 is probably due to the formation of a very smooth and compact tribological layer on its surface. This issue may be explained by considering the relation between the friction coefficient and the interfacial shear strength shown in Eq. (2) [42]:

$$\mu = \frac{1}{\sqrt{\alpha[(\frac{\tau_0}{\tau_i})^2 - 1]}} \tag{2}$$

where, μ is the friction coefficient, α is a constant, and τ_i and τ_0 are shear strength of the interface and bulk, respectively. As seen, the friction coefficient is inversely proportional to the tribolayer shear strength (τ_i). Therefore, the formation of tribolayer is likely to reduce the AFC.

However, it seems that the consumption of energy due to the initiation and propagation of subsurface cracks (Fig. 14(b)) increased the fluctuation of the graph.

4. Conclusion

The effects of the surface FH on the microstructure and the tribological properties of L605 alloy using a tungsten carbide tool under different sliding speeds of 500, 800, 1100, 1400, 1700, and 2000 mm/min for 2, 5, 10, 20, and 30 passes were studied. The following results can be drawn:

1. Applying FH promoted the ε-martensitic transformation (transformation of the quasi-stable γ-FCC to the stable ε-HCP) up to a depth of about 500 μm beneath the processed surface of L605 alloy. Depending on the number of FH passes, the surface hardness increased up to 100%.
2. the FH process improved the wear resistance of L605 alloy. The best result was obtained in the case of the sample processed at the sliding speed of 1700 mm/min for 5 passes. Under the applied pressures of 0.25, 0.5, and 1 MPa, the wear rate of this sample was lower than that of the base sample by about 36, 43, and 53%, respectively. The average friction coefficient and the friction coefficient fluctuation range of 1700-5 sample was lower than those of the base alloy by 33 and 78%, respectively.
3. Increasing the number of the sliding passes up to 30 led to a substantial increase in the alloy hardness. However, after 5 passes of FH, lateral microcracks appeared on the surface. During the sliding wear, these cracks destabilized the tribolayer over the worn surface and encouraged the wear of the alloy by delamination and abrasion mechanisms.

Conflict of Interests

The authors have no conflicts of interest to declare.

Funding

This research has not received any specific fund to be declared here.

5. References

[1] P. Crook, Cobalt and Cobalt Alloys, ASM Handbook, Properties Selection of Nonferrous Alloy and Special-Purpose Material, ASM International, USA, 1990, pp. 1416-1421.

[2] R.V. Marrey, R. Burgermeister, R.B. Grishaber, R.O. Ritchie, Fatigue and life prediction for cobalt-chromium stents: A fracture mechanics analysis, *Biomaterials*, 27(9) (2006) 1988-2000.

[3] ASTM F90, Wrought cobalt-20chromium-15tungsten-10nickel alloy surgical implant application (UNS R30605), ASTM International, 2014.

[4] ASTM F1091, Wrought cobalt-20chromium-15tungsten-10nickel alloy surgical fixation wire (UNS R30605), ASTM International, 2002.

[5] L.M. de Andrade, C. Paternoster, V. Montaño-Machado, G. Barucca, M. Sikora-Jasinska, R. Tolouei, S. Turgeon, D. Mantovani, Surface modification of L605 by oxygen plasma immersion ion implantation, *MRS Communications*, 8(4) (2018) 1404-1412.

[6] P.A.G. Rashidi, H. Arabi, S.M. Abbbasi, Effect of cold-rolling on mechanical properties of Haynes 25 cobalt-based superalloy, *Journal of Metallurgical and Materials Engineering*, 23(1) (2017) 31-45.

[7] S.M. Arab, A. Haghighi M. Khajepour, Y. Jalalizadeh, M.M. Tavallayi, Conjoint influence of heat treatment, hot deformation and cold working on the microstructure and mechanical response of a Co-based superalloy, *Iranian Journal of Materials Forming*, 8(3) (2021) 34-45.

[8] K. Salonitis, Grind hardening process, Cham, Heidelberg: Springer International Publishing, New York, 2015.

[9] V. Schulze, Modern mechanical surface treatment: states, stability, effects, John Wiley & Sons, 2006.

[10] L.N. López de Lacalle, A. Lamikiz, J. A. Sánchez, J.L. Arana, The effect of ball burnishing on heat-treated steel and Inconel 718 milled surfaces, *The International Journal of Advanced Manufacturing Technologies*, 32 (2007) 958-968.

[11] J. Huuki, S.V.A. Laakso, Surface improvement of shafts by the diamond burnishing and ultrasonic burnishing techniques, *International Journal of Machining and Machinability of Materials*, 19(3) (2017) 246-259.

[12] V. Schulze, F. Bleicher, P. Groche, Y.B. Guo, Y.S. Pyun, Surface modification by machine hammer peening and burnishing, *Cirp Annals*, 65(2) (2016) 809-832.

[13] S. Yanga, D.A. Puleob, O.W. Dillon, I.S. Jawahir, Surface layer modifications in Co-Cr-Mo biomedical alloy, *Procedia Engineering*, 19 (2011) 383-388.

[14] F. Shahriyari, R. Taghiabadi, A. Razaghian, M. Mahmoudi, Effect of friction hardening on the surface mechanical properties and tribological behavior of biocompatible Ti-6Al-4V alloy, *Journal of Manufacturing Processes*, 31 (2018).

[15] A.V. Makarov, L.G. Korshunov, I.Y. Malygina, I.L. Solodova, Raising the heat and wear resistances of hardened carbon steels by friction strengthening treatment, *Metal Science and Heat Treatment*, 49 (2007) 150-156.

[16] A.V. Makarov, R.A. Savrai, N.A. Pozdejev, S.V. Smirnov, D.I. Vichuzhanin, L.G. Korshunov, I.Y. Malygina, Effect of hardening friction treatment with hard-alloy indenter on microstructure, mechanical properties, and deformation and fracture features of constructional under static and cyclic tension, *Surface and Coating Technology*, 205(3) (2010) 841-852.

[17] A.V. Makarov, P.A. Skorynina, A.S. Yurovskikh, A.L. Osintseva, Effect of the technological conditions of frictional treatment on the structure, phase composition and hardening of metastable austenitic steel, *AIP Conference Proceedings*, 1785(1) (2016).

[18] A. Khaksaran, R. Taghiabadi, M. Jafarzadegan, Tribological properties of surface friction hardened AISI 316L steel, *Transactions of the Indian Institute of Metals*, 74(8) (2021) 1979-1989.

[19] S. Yu, Y. Wan, C. Liu, Z. Chen, X. Zhou, Twinning-induced abnormal strain rate sensitivity and indentation creep behavior in nanocrystalline Mg alloy. *Materials*, 14(22) (2021) 7104.

[20] G.E. Totten, ASM handbook: Volume 18, Friction, lubrication and wear technology, ASM International, Cleveland, 1992.

[21] A.H. Almasri, G.Z. Voyiadjis, Effect of strain rate on the dynamic hardness in metals, *Journal of Engineering Materials and Technology*, 129(4) (2007) 505-512.

[22] V.M. Heydari, M. Sedighi, M. Mondali, Mechanical properties and microstructural evaluation of AA5083/Al_2O_3 composites fabricated by warm accumulative roll bonding, *International Journal of Advanced Design and Manufacturing Technology*, 9(4) (2016) 13-22.

[23] T.B. Tavares, D.G. Rudrigues, D.B. Santos, Effect of warm rolling and annealing on microstructure, texture, and mechanical properties of a 2205 duplex stainless steel, *Steel Research International*, 91(4) (2020) 1900543.

[24] F. A. Mohamed, A dislocation model for the minimum grain size obtainable by milling, *Acta Materialia*, 51(14) (2003) 4107-4119.

[25] C. Perrin, W.M. Rainforth, Work hardening behavior at the worn surface of Al–Cu and Al–Si alloys. *Wear*, 203 (1997) 171-179.

[26] J. Favre, Recrystallization of L-605 cobalt superalloy during hot-working process, Doctoral dissertation, INSA de Lyon; Tōhoku Daigaku (Sendai, Japan), 2012.

[27] R. Wang, R. Wang, D. Chen, G. Qin, E. Zhang, Novel CoCrWNi alloys with Cu addition: Microstructure, mechanical properties, corrosion properties and biocompatibility, *Journal of Alloys and Compounds*, 824 (2020) 153924.

[28] B.S. Lee, H. Matsumoto, A. Chiba, Fractures in tensile deformation of biomedical Co–Cr–Mo–N alloys, *Materials Letters*, 65(5) (2011) 843-846.

[29] Z. Zhu, L. Chen, Effect of annealing on microstructure and mechanical properties of biomedical hot-rolled Co-Cr-W-Ni alloy, *Materials Research Express*, 6(12) (2019) 126511.

[30] D.L. Klarstrom, Wrought cobalt-base superalloys, *Journal of Materials Engineering and Performance*, 2 (1993) 523-530.

[31] H. Fujita, S. Ueda, Stacking faults and f.c.c. (γ) → h.c.p. (ε) transformation in 188-type stainless steel, *Acta Metallurgica*, 20(5) (1972) 759-767.

[32] H.M. Tawancy, V.R. Ishwar, B.E. Lewis, On the fcc → hcp transformation in a cobalt-base superalloy (Haynes alloy No. 25), *Journal of Materials Science Letters*, 5(3) (1986) 337-341.

[33] Y. Koizumi, S. Suzuki, K. Yamanaka, B.S. Lee, K. Sato, Y. Li, S. Kurosu, H. Matsumoto, A. Chiba, Strain-induced martensitic transformation near twin boundaries in a biomedical Co–Cr–Mo alloy with negative stacking fault energy, *Acta Materialia*, 61(5) (2013) 1648-1661.

[34] M. Knezevic, J.S. Carpenter, M.L. Lovato, R.J. McCabe, Deformation behavior of the cobalt-based superalloy Haynes 25: Experimental characterization and crystal plasticity modeling, *Acta Materialia*, 63 (2014) 162-168.

[35] Y.S. Mao, L. Wang, K.M. Chen, S.Q. Wang, X.H. Cui, Tribo-layer and its role in dry sliding wear of Ti–6Al–4V alloy, *Wear*, 297(1-2) (2016) 1032-1039.

[36] T. Vitu, A. Escudeiro, T. Polcar, A. Cavaleiro, Sliding properties of Zr-DLC coatings: The effect of tribolayer formation. *Surface and Coatings Technology*, 258 (2014) 734-745.

[37] S. Pouladvand, R. Taghiabadi, F. Shahriyari, Investigation of the tribological properties of AlxSi-1.2Fe(Mn) (x=5-13 wt.%) alloys. *Journal of Materials Engineering and Performance*, 27(7) (2018) 3323-3334.

[38] Z. Nouri, R. Taghiabadi, Tribological properties improvement of conventionally-cast Al-8.5Fe-1.3V-1.7Si alloy by multi-pass friction stir processing, *Transactions of Nonferrous Metals Society of China*, 31(5) (2021) 1262-1275.

[39] M. Fekri Soustani, R. Taghiabadi, M. Jafarzadegan, F. Shahriyari, A. Rahmani, Improving the tribological properties of Al-7Fe-5Ni alloys via friction stir processing, *Journal of Tribology*, 141(12) (2019) 121602.

[40] X. Tong, T. Shen, X. Zhou, J. Zeng, J. Tao, K. Munir, Y. Li, S. Huang, X. Wu, J. Ma, J. Lin, C. Wen, Biodegradable Zn–Cu–Li alloys with ultrahigh strength, ductility, antibacterial ability, cytocompatibility, and suitable degradation rate for potential bone-implant applications, *Smart Materials in Manufacturing*, 1 (2023) 100012.

[41] S.J. Lee, Y.K. Lee, A. Soon, The austenite/ε martensite interface: A first-principles investigation of the fcc Fe (111)/hcp Fe (0001) system. *Applied Surface Science*, 258(24) (2012) 9977-9981.

[42] H. Hirani, Fundamentals of engineering tribology with applications, Cambridge University Press, Delhi, India, 2016.